

pubs.acs.org/JPCC Article

# Mixed Organic Cation in Chiral Two-Dimensional Organic—Inorganic Hybrid Metal Halides—An Ab Initio Study of Nonlinear Optical (NLO) Properties

Xiyue Cheng, S. Muthukrishnan, Hanxiang Mi, Shuiquan Deng, Goncagül Serdaroğlu, R. Vidya, and Alessandro Stroppa\*



Cite This: J. Phys. Chem. C 2024, 128, 11392-11400



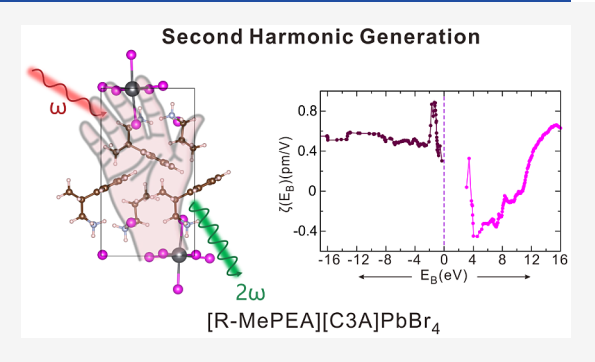
**ACCESS** I

III Metrics & More

Article Recommendations

Supporting Information

ABSTRACT: The mixing of organic cations represents yet another direction to explore in the field of chiral organic-inorganic hybrid metal halides (OIHMH). Here, we perform structural optimizations, electronic structures, and nonlinear optical (NLO) studies using density functional theory of two recently synthesized chiral OIHMHs, [R-MePEA][C3A]-PbBr<sub>4</sub> and [R-MePEA][C4A]PbBr<sub>4</sub>, with mixed chiral arylammonium and achiral alkylammonium cations. We find that the noncovalent weak interactions (e.g., Br...NH interactions) play an important role in the description of these OIHMHs. Our study further indicates that the two noncentrosymmetric compounds exhibit relatively wide bandgaps (~3.5 eV), strong second harmonic generation (SHG) responses ( $\sim 0.5-1.5 \times 1.5$ KDP), and moderate birefringence (~0.088 at 1064 nm), indicating



possible applications for NLO materials. Atom response theory analysis reveals that the SHG responses are determined mainly by the occupied Br 3p nonbonding orbitals as well as by the unoccupied Pb 5p orbitals, which shows the important contribution of the inorganic PbBr<sub>4</sub> layer to the nonlinear optical properties.

#### 1. INTRODUCTION

Chirality is a unique geometrical phenomenon that has received great importance in the fields of physics, chemistry, and materials science. If a specific molecule cannot overlap with its mirror image by proper symmetry operations, such as translations and/or rotations, the molecule is chiral, and the mirror images are called enantiomers. The research on chiral systems is mainly related to organic synthesis and applications in medicinal chemistry<sup>1,2</sup> since critical molecules in the living body are in the chiral framework.3 In the past, the chiral inversion pathway of poly(BBPFA) structure was investigated by the atomistic approach using chirality-based variables to get the free energy profile in this conversion. Furthermore, the parity-violation energy due to weak forces,  $\Delta E_{\rm pv}$  (total electronic energy difference of two enantiomers) and the ECM (electronic chirality measure) relationship were reported, and the authors suggested that the weak forces producing parity-violating effects can be critical to understanding the biological homochirality phenomenon.<sup>5</sup> The presence of chirality can provide considerable flexibility in the functional material design due to its noncentrosymmetric nature.

1.1. Organic-Inorganic Hybrid Metal Halides. (OIHMHs) have great technological potential in the fields of photovoltaics, LEDs, and other optoelectronic applications. Two-dimensional (2D) OIHMHs attracted much research interest due to their unique characteristics, such as good

thermal and chemical stabilities.<sup>6</sup> They have interesting electronic properties such as tunable bandgaps, long charge carrier lifetimes, mobility, higher absorption coefficients, and high photoluminescence. By carefully choosing the proper organic spacer cation in 2D OIHMHs, the tuning of their electrical and optical properties is achieved.<sup>8</sup> Mixing more than one cation leads to a new possible strategy to engineer the optoelectronic properties of 2D OIHMHs. 9,10 In particular, mixing more than one organic cation was recently explored by Yan et al.<sup>11</sup> who studied aromatic ammonium-based 2D OIHMHs. Qiu et al. studied the Ruddlesdan-Popper phases on tin-based mixed organic spacer cations (n-butylamine and phenethylamine) for solar cell application. 12 Similarly, Lian et al. fabricated the butylammonium and methylammonium mixed spacer cation 2D OIHMHs, oriented with a grain size larger than 1  $\mu$ m.<sup>13</sup> Mixing different organic cations in 2D OIHMHs may significantly modify their properties, leading to

Received: April 18, 2024 Revised: June 11, 2024 Accepted: June 17, 2024 Published: June 27, 2024





© 2024 American Chemical Society

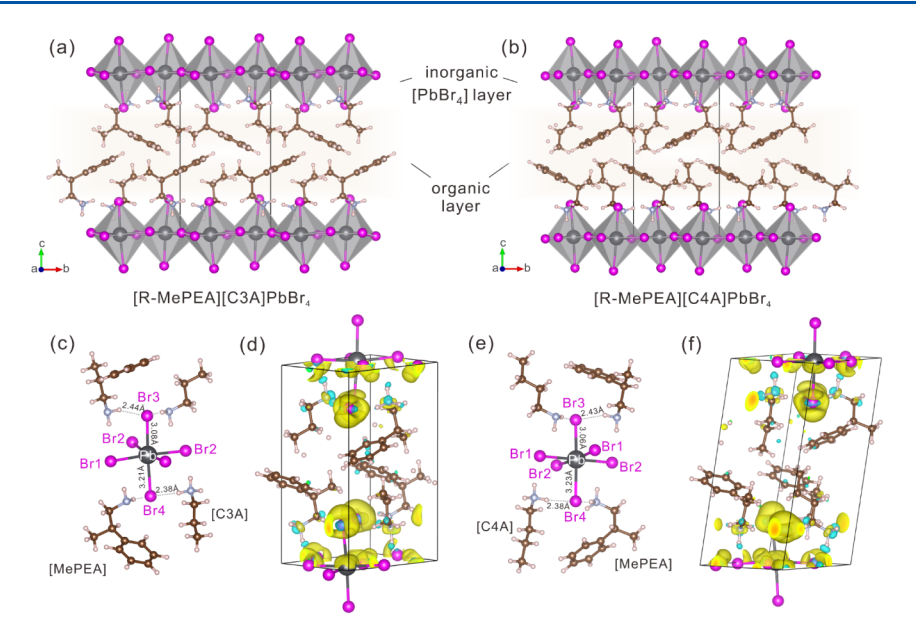


Figure 1. 2D layered structures of [R-MePEA][C3A]PbBr<sub>4</sub> (a) and [R-MePEA][C4A]PbBr<sub>4</sub> (b). The coordination environment of PbBr<sub>6</sub> octahedron and the Br···NH weak interactions (c, e) together with the corresponding calculated charge density differences (d, f) for these two compounds, respectively.

a reduction in the trap state density, incrementing solar cell efficiency, and improved structural stability.<sup>14</sup>

The mixing of the chiral organic cations with the achiral organic ones in order to "chiralize" 2D OIHMHs is considered another emerging area of research. The resulting chirality transfer between chiral organic cations and the framework results in chiral 2D OIHMHs, thus allowing for chiraloptoelectronic applications and spintronic properties. 16 Kim et al. studied the chiral-cation-induced spin selectivity of roomtemperature LEDs, where the organic layer injects the spinpolarized holes into the halide perovskite.<sup>17</sup> Furthermore, the presence of chiral ligands in the lead halide framework enables strong circularly polarized light emission and detection. 18 Ishii et al. used helical lead-halide 1D perovskite with chiral organiccation-based photodiodes for the detection of circularly polarized light. Here, circularly polarized light detection with 1D perovskite has the highest polarization discrimination ratio of 25.4, which is larger than other conventional devices. 19 Yang et al. synthesized the first 2D perovskite ferroelectrics by incorporating homochiral cations into the 2D OIHMHs and studied the material by crystal structure analysis and circular dichroism spectra.<sup>20</sup> The good structural and chemical properties of the halide perovskites enabled their strong application in the field of nonlinear optics (NLO).<sup>21-25</sup> NLO materials play a crucial role in modern laser technology as electro-optical materials for optical modulators, Q-switches, detectors, and frequency converters because of their nonlinear interactions with incident light.

Recently, Yan et al. 26 experimentally synthesized the single-layer thick 2D lead bromide HOIPs comprising chiral aryl organic cation part (MePEA: methylphenethylammonuim) and achiral alkyl cations (C3A: propylammonium or C4A: butylammonium). They studied the mixed alkyl-aryl cations with a 1:1 molar ratio and characterized the structure for the first time by analyzing the role of the CH $\bullet\bullet\bullet\pi$  interaction in the structural formation of chiral mixed 2D HOIPs.

In this work, we study the structural, electronic structures, and NLO properties of the chiral mixed cation 2D HOIPs, [R-

MePEA][C3A]PbBr<sub>4</sub> and [R-MePEA][C4A]PbBr<sub>4</sub>. <sup>26</sup> We reveal the important role of Br···NH noncovalent interactions between the inorganic and organic layers in the description of the 2D-layered HOIPs. Our study further suggests that both OIHMHs show large SHG responses (i.e.,  $\sim$ 1.49 and 0.53 ×  $d_{\rm eff}^{\rm KDP}$ ) among the reported lead-containing OIHMHs, which implies their possible application as NLO materials. Besides, the origin of the large SHG response is found to be from the inorganic groups rather than the organic parts. For completeness, in the Supporting Information (SM), we also study the optical rotatory dispersion (ORD) and electronic circular dichroism (ECD) spectra of the neutral and cationic MePEA enantiomers.

#### 2. METHODS

The structural and electronic properties of [R-MePEA][C3A]-PbBr₄ and [R-MePEA][C4A]PbBr₄ were calculated by using the density functional theory (DFT) and the projector augmented wave (PAW) method implemented in the Vienna Ab initio Simulation Package (VASP).<sup>27-29</sup> The generalized gradient approximation (GGA) of the exchange-correlation potential in the form of the Perdew-Burke-Ernzerhof (PBE) was used throughout this work.<sup>30</sup> The employed PAW-PBE pseudopotentials of elements Pb, Br, C, N, and H treat  $5d^{10}6s^26p^2$ ,  $4s^24p^5$ ,  $2s^22p^2$ ,  $2s^22p^3$ , and 1s as the valence states, respectively.<sup>31</sup> The plane wave cutoff energy for the expansion of wave functions was set at 600 eV with a dense k-point mesh of  $7 \times 7 \times 4$  for both compounds. The conjugate-gradient algorithm as implemented in the VASP code was used in all structural relaxations. In this work, the atomic positions were all allowed to relax to minimize the internal forces while keeping the unit cell lattice constants to experimental values. The convergence criteria for the energy differences (0.1 meV) and stress tensors (≤0.005 eV/Å) were achieved.

The second-order NLO properties were calculated by employing the "sum over states (SOS)" methods using the code (ARTAROP) that we have recently developed<sup>32</sup> based on the calculated electronic structures obtained from the

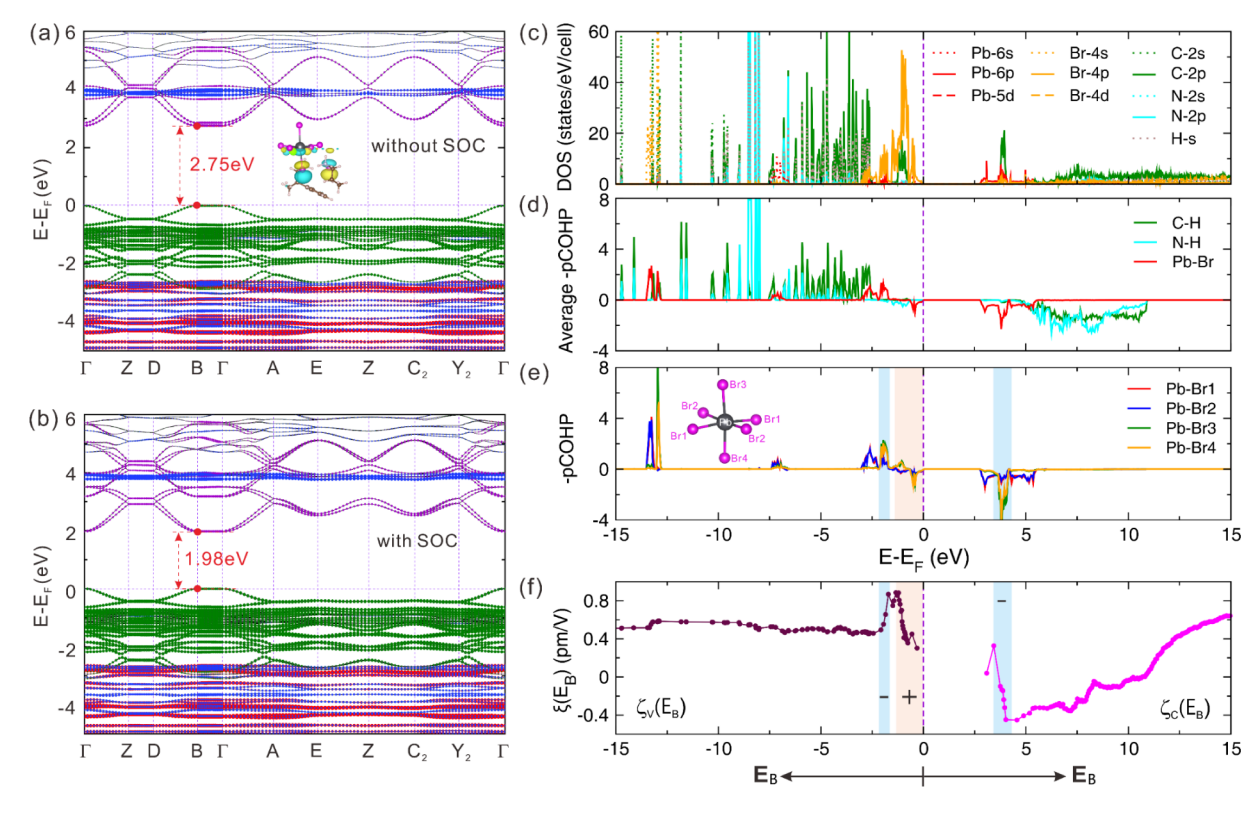


Figure 2. Band structures of [R-MePEA][C3A]PbBr<sub>4</sub> (a, b) without and with SOC.  $\Gamma$ =(0, 0, 0), Z = (0, 0.5, 0.5), D = (0, 0.5), D = (0.5), D = (0

VASP<sup>27-29</sup> optical modules. The SOS formalism for secondorder susceptibility was derived by Aversa and Sipe<sup>33</sup> and later modified by Rashkeev et al. 34,35 and Sharma et al. 36,37 As the DFT electronic structure calculations underestimate bandgaps, the scissor operation<sup>38</sup> was used to increase the energies of the unoccupied states from those of the occupied ones to have the HSE06<sup>39-41</sup> bandgaps. The powder SHG response, the effective  $d_{\text{eff}}^p$ , an average SHG coefficient over all possible orientations of the powder crystals are estimated from the formula derived by Kurtz-Perry<sup>42</sup> and Cyvin et al.<sup>43</sup> based on the calculated nonzero SHG tensor elements. To evaluate the individual atom and orbital contributions to the SHG components, the atom response theory (ART) based on the partial response functional (PRF) was used (see SM).<sup>30</sup> Finally, the ORD and ECD spectroscopic computations of both neutral and cationic MePEA enantiomers were performed by G16W software, 44 at B3LYP/6-311++G(d,p). $^{45,46}$  The Chem3D 17.1<sup>47</sup> program was used to calculate the Connolly solvent-excluded volumes of MePEA enantiomers and compared with the corresponding data to confirm the electronic structures. The Gauss View 6.0.16 package<sup>48</sup> was used for analysis and illustration of the computed results (See SM).

## 3. RESULTS AND DISCUSSION

**3.1. Structural Optimization.** The relaxed structures for [R-MePEA][C3A]PbBr<sub>4</sub> and [R-MePEA][C4A]PbBr<sub>4</sub> are shown in Figure 1. We also compared the experimental crystal structures with the calculated ones using Bilbao crystallographic server database<sup>48</sup> as presented in Table S1, showing the degree of lattice distortion, the maximum displacement

between the atomic positions, the arithmetic mean value, and the overall measurement of similarity. The calculated values of structure comparison (with the experimental values) for both compounds in the PBE-GGA and DFT-D2 correction

suggest a good agreement of our optimized structure models with the experimental structures. After the relaxation, the bond lengths for Pb–Br, C–C, N–C, and N–H slightly increased compared to the experimental values at the PBE-GGA level, as shown in Table S2. Such an increase is further weakly enhanced when considering the van der Waals dispersion correction. Note that the differences in the measurement of similarity at the two computation levels are so small that they do not give statistically significant results. Generally, the inclusion of weak noncovalent interactions leads to a better structural description in organic and inorganic hybrid systems.

Both compounds crystallize in the NCS space group P2<sub>1</sub> (Figure 1a,b). Within each unit cell, Pb atoms have one crystallographically unique site, whereas the Br, N, C, and H atoms occupy 4, 2, 12, and 24 independent crystallographic positions, respectively. All atoms are at special Wyckoff positions of 2a. The Pb atoms are coordinated with six Br atoms, of which two Br1 and two Br2 are located in the ab plane, Br3 and Br4 are along the c direction, forming distorted PbBr<sub>6</sub> octahedra (Figure 1c,e). Within the ab plane, neighboring Pb-centered octahedra are connected by sharing Br1 and Br2 atoms with bond lengths around 3.06 Å, leading to an inorganic PbBr<sub>4</sub> layer. For the ones along the c axis, the Pb-Br3 distances (~3.07 Å) are similar to those of the inner ab plane Pb-Br bonds, while they are all obviously shorter than Pb-Br4 distances ( $\sim$ 3.27 Å), indicating weaker Pb-Br4 bonding interactions. The formation of such distorted PbBr<sub>6</sub>

Table 1. Calculated Values of  $E_g^{\text{PBE}}$ ,  $E_g^{\text{SOC}}$ ,  $E_g^{\text{HSE}}$ , Static SHG Tensor  $d_{ij}$ , Static Effective Response  $d_{\text{eff}}$  and Birefringence at 1064 nm

material	$E_g^{\mathrm{PBE}}$ (eV)	$E_g^{SOC}$ (eV)	$E_g^{ m HSE}$ (eV)	$d_{ij} \; (\mathrm{pm/V})$	$d_{\rm eff}~({ m pm/V})$	$\Delta n$ at 1064 nm
[R-MePEA][C3A]PbBr <sub>4</sub>	2.75	1.98	3.53	$d_{14} = 0.50$ $d_{16} = -0.35$ $d_{21} = -0.27$ $d_{22} = 0.25$ $d_{23} = 0.26$ $d_{25} = 0.55$ $d_{34} = 0.26$ $d_{36} = 0.42$	$0.493 \ (1.49 \times d_{\text{eff}}^{\text{KDP}})$	0.089
[R-MePEA][C4A]PbBr <sub>4</sub>	2.76	1.97	3.54	$d_{14} = 0.20$ $d_{16} = 0.08$ $d_{21} = 0.14$ $d_{22} = -0.09$ $d_{23} = -0.06$ $d_{25} = 0.21$ $d_{34} = -0.11$ $d_{36} = 0.14$	$0.173 \ (0.53 \times d_{\text{eff}}^{\text{KDP}})$	0.086

octahedra may be induced by the second-order Jahn-Teller (SOJT) distortion.

The inorganic and organic layers are stabilized through noncovalent interactions, such as Br...NH interactions, which exist between Br atoms and the terminal NH<sub>3</sub> of the R-MePEA cation and C3 or C4 alkyl cation, respectively. The distances of Br...NH interaction in [R-MePEA][C3A]PbBr<sub>4</sub> and [R-MePEA][C4A]PbBr<sub>4</sub> are very similar, around 2.39-2.86 Å. These values are less than the maximum distance (3.20 Å) to have such weak interactions (1.05 times the sum of the van der Waals radii of H and Br atoms), indicating the presence of Br... NH interactions. The noncovalent weak interactions are further evidenced by the calculated charge density differences (CDD) by using  $\Delta \rho = \rho_{\rm compound} - \rho_{\rm inorganic} - \rho_{\rm organic}$  where  $\rho_{\rm compound}$  denotes the total charge density of [R-MePEA]-[C3A]PbBr<sub>4</sub> or [R-MePEA][C4A]PbBr<sub>4</sub>, and  $\rho_{\text{inorganic}}$  and  $\rho_{\text{organic}}$  represent the charge density of the inorganic [PbBr<sub>4</sub>] layer and the organic mixed alkyl-aryl layer, respectively, as displayed in Figure 1d,f. The CDD results clearly show the interlayer charge transfer in both compounds, in which the majority of charges transfer from the N-H groups of [R-MePEA] and [C3A] ([C4A]) to the PbBr<sub>6</sub> octahedra. Besides, the organic cations are also stabilized through weak interactions, such as  $CH \cdots \pi$  interactions, which were discussed in detail by Yan et al.26 It can be seen that the weak noncovalent interactions play an essential role in the formation of these 2D hybrid perovskites.

**3.2. Electronic Structures.** The electronic structures are described at the level of PBE-GGA, including spin—orbit coupling (SOC). The direct

PBE bandgaps ( $E_g^{PBE}$ ) at B=(0,0,0.5) for [R-MePEA][C3A]PbBr<sub>4</sub> and [R-MePEA][C4A]PbBr<sub>4</sub> are calculated as 2.75 and 2.76 eV, respectively. The SOC effect causes a band split of Pb-6p states at Z and D points, which further reduces the  $E_g^{PBE}$  to 1.98 and 1.97 eV ( $E_g^{SOC}$ ), respectively (Figures 2a,b and S1). Note that, generally, both the PBE or PBE-SOC would yield band gaps relatively smaller with respect to the experimental gaps due to the well-known incorrect estimation of the quasi-particle energies, and we also apply the hybrid functional HSE06 calculations with mixing parameter  $\alpha=0.25$  to obtain the  $E_g^{HSE}$ , 3.53 and 3.54 eV, respectively. For both compounds, the valence band maximum (VBM) is mainly

dominated by the Br 4p and Pb 6s states, while the conduction band minimum (CBM) is primarily composed of unoccupied Pb 6p states. The C 2p, N 2p, and H p-like states from the organic part mainly occupied the VBs at  $\sim\!\!2.5$  eV below the Fermi level, while some relatively localized C 2p states lie at  $\sim\!\!4.0$  eV in the CBs. This clearly suggests that the bands near the Fermi level are dominated by orbitals from the inorganic PbBr<sub>4</sub> layer rather than the organic molecules in these two compounds.

The calculated partial density of states (PDOS) (Figures 2c, S2a, and S3) for both compounds shows very similar features. The top valence bands (-2.3 eV to the Fermi level) consist of mainly Br 4p states and a weak mixing with C 2p states, while those between -15 and -2.3 eV are mainly composed of a large amount of hybridized C 2p and H s as well as N 2p and H s states. Relatively weak Pb 5p valence states can be found around -2.0 eV, while the inner Pb 6s and 5d orbitals mainly localize at -7.0 and -16.0 eV, respectively. The bottom of the conduction bands ( $E_g$ -5.5 eV) is primarily made up of Pb-5p states and C-2p states, while the bands between 5.5 and 20 eV result from the unoccupied states of C, N, H, and Br atoms.

**3.3. Bonding Interactions.** To elucidate the bonding characteristics of the compound, crystal orbital Hamiltonian population (COHP)<sup>49,50</sup> analysis was performed (Figures 2d,e and S2b). As expected, the bonding characteristics for both [R-MePEA][C3A]PbBr<sub>4</sub> and [R-MePEA][C4A]PbBr<sub>4</sub> are also almost similar. The Br-4p states at the top valence bands are nonbonding states. Strong bonding interactions between the states of Br 4p and Pb 6p occurred in the region around -2.0 eV, while relatively weak interactions between Br 4p and Pb 6s can be found around ~-7.0 eV. C-H and N-H p-s bonding interactions overlap over a wide energy range and the bonding strengths are found to be stronger than those of the Pb-Br interactions. Understanding the bonding and nonbonding energy regions is crucial for interpreting the origin of SHG, as discussed below.

**3.4. Second Harmonic Generation (SHG).** Because of the point group of  $C_2$ , the SHG tensor for [R-MePEA][C3A]-PbBr<sub>4</sub> and [R-MePEA][C4A]PbBr<sub>4</sub> has eight nonzero components, e.g.,  $d_{14}$ ,  $d_{15}$ ,  $d_{21}$ ,  $d_{22}$ ,  $d_{23}$ ,  $d_{25}$ ,  $d_{34}$ , and  $d_{36}$ , as presented in Table 1. The Kleinman symmetry (KS), i.e.,  $d_{14}$  =

Table 2. Contributions of the Individual Atoms to the Largest SHG Component  $d_{25}$  of [R-MePEA][C3A]PbBr<sub>4</sub> and [R-MePEA][C4A]PbBr<sub>4</sub>.

material	atom	$W_A$	$A_{ au}$	$C_A$	${^{ ext{VB}}}A_{ au}$	$^{\mathrm{CB}}\mathrm{A}_{ au}$	${}^{\mathrm{VB}}{}_{s}\mathrm{A}_{ au}$	$^{\mathrm{VB}}{}_{\mathrm{p}}\mathrm{A}_{\mathrm{\tau}}$	$^{\mathrm{VB}}{}_{\mathrm{d}}\mathrm{A}_{\mathrm{ au}}$	$^{\mathrm{CB}}{}_{\mathrm{s}}\mathrm{A}_{\mathrm{\tau}}$	$^{\mathrm{CB}}_{}\mathrm{p}}\mathrm{A}_{ au}$	$^{\mathrm{CB}}{}_{\mathrm{d}}\mathrm{A}_{ au}$
[R-MePEA][C3A]PbBr <sub>4</sub>	Pb	2	19.9	39.8	7.2	12.7	5.3	-1.0	3.0	0.1	12.1	0.5
	Br1	2	5.3	10.7	1.4	3.9	-1.6	3.0	0.0	1.0	1.8	1.1
	Br2	2	4.3	8.7	0.6	3.7	-1.6	2.2	0.0	1.1	1.6	1.1
	Br3	2	1.8	3.5	2.4	-0.6	-0.2	2.6	0.0	-0.2	-0.9	0.5
	Br4	2	5.8	11.6	5.9	-0.2	-0.1	6.1	0.0	-0.3	-0.4	0.5
	C	24	0.4	8.7	0.5	-0.1	0.0	0.5	0.0	0.2	-0.3	0.0
	N	4	1.4	5.6	0.5	0.9	0.0	0.5	0.0	0.1	0.8	0.0
	Н	48	0.2	11.4	0.0	0.2	0.0	0.0	0.0	0.1	0.1	0.0
[R-MePEA][C4A]PbBr <sub>4</sub>	Pb	2	26.4	52.7	5.2	21.2	3.9	-0.8	2.1	0.1	20.7	0.3
	Br1	2	7.4	14.8	2.5	4.9	-0.9	3.4	0.0	1.5	2.5	1.0
	Br2	2	8.3	16.6	3.2	5.1	-0.9	4.1	0.0	1.4	2.7	1.0
	Br3	2	-2.6	-5.2	-1.9	-0.7	-0.1	-1.7	0.0	-0.2	-0.8	0.3
	Br4	2	2.3	4.7	2.9	-0.6	0.0	2.9	0.0	-0.2	-0.5	0.2
	C	26	0.2	6.1	0.5	-0.3	0.2	0.3	0.0	0.1	-0.4	0.0
	N	4	-0.3	-1.3	-0.7	0.4	0.0	-0.7	0.0	0.1	0.3	0.0
	Н	52	0.2	11.6	0.1	0.1	0.1	0.0	0.0	0.1	0.0	0.0

 $<sup>^</sup>aA_{\tau}$  is the contribution (in %) from a single atom  $\tau$ , and CA is that from all atoms of the same type.  $^{VB}_{A\tau}$  is the contribution (in %) of the VBs, and  $^{CB}_{A\tau}$  is the contribution from the CBs. The contributions from the s, p, and d states of the atom  $\tau$  to  $^{VB}_{A\tau}$  and  $^{CB}_{A\tau}$  are also shown. WA refers to the number of the same type of atoms (i.e., on the same Wyckoff site) in a unit cell. As the  $A\tau$  for C, N, and H atoms are very small, only the total averaged value is given.

 $d_{25} = d_{36}$ ,  $d_{16} = d_{21}$  and  $d_{23} = d_{34}$ , is not strictly followed in these two compounds. The breaking down of the

Kleinman symmetry means that the polarization directions of the mixed pump light and that of the exit light cannot be permuted, indicating the occurrence of dynamic anisotropy in the SHG response of the lower-symmetry structure. 51 For this reason, KS is not enforced in calculating the NLO properties in this work. The static effective SHG values of [R-MePEA]-[C3A]PbBr<sub>4</sub> and [R-MePEA][C4A]PbBr<sub>4</sub> were calculated as 0.493 and 0.173 pm/V, respectively (i.e.,  $\sim$ 1.49 and 0.53  $\times$  $d_{\text{eff}}^{\text{KDP}}$ ). Note that the SHG response of [R-MePEA][C3A]-PbBr<sub>4</sub> is stronger than that of Potassium Dihydrogen Phosphate (KDP, static  $d_{\text{eff}}^{\text{KDP}}$  = 0.33 pm/V) and is comparable or stronger than that of some other OIHMHs, such as TMIM-PbCl<sub>3</sub> (powder SHG intensity  $I_{powder}^{2\omega} \sim 1 \times KDP$ ), 52 MHy<sub>2</sub>PbBr<sub>4</sub> ( $I_{\rm powder}^{2\omega} \sim 0.1 \times {\rm KDP}$ ), MHyPbBr<sub>3</sub> ( $I_{\rm powder}^{2\omega} \sim$  $0.18 \times \text{KDP}$ ), 54 [CH<sub>3</sub>(CH<sub>2</sub>)<sub>3</sub>NH<sub>3</sub>]<sub>2</sub>(CH<sub>3</sub>NH<sub>3</sub>)Pb<sub>2</sub>Br<sub>7</sub> ( $I_{\text{powder}}^{2\omega}$  $\sim 0.4 \times \text{KDP}$ , so and (MePEA)<sub>1.5</sub>PbBr<sub>3.5</sub>(DMSO)<sub>0.5</sub> ( $d_{\text{eff}} =$ 0.68 pm/V).<sup>56</sup> Besides, the birefringence is also evaluated, as the phase matching condition is important for the efficiency of an SHG process. The calculated birefringence value  $(\Delta n)$  for [R-MePEA][C3A]PbBr<sub>4</sub> and [R-MePEA][C4A]PbBr<sub>4</sub> are 0.089 and 0.086, respectively, at 1064 nm which fall in the range of technical applications (0.03-0.10). Therefore, based on the calculated relatively wide band gaps, strong SHG responses, and moderate birefringence, it can be inferred that these two OIHMHs are potentially suitable for nonlinear optical applications, thus suggesting that further studies are needed in order to find mixed chiral OIHMHs with optimized NLO responses. The calculated specific rotation degrees 57-59 from 150 to 1064 nm and related ORD and ECD spectra for MePEA enantiomers are given in Tables S3,S4 and Figure S4.

The origin of the SHG responses is further investigated by employing ART analysis.<sup>30</sup> The ART analysis enables one to determine the contributions of individual atomic orbitals and, hence, those of individual atoms to the SHG coefficients using

the PRF method (see SM for details). Shown in Figures 2f and S2c are the PRFs,  $\zeta_V(E_B)$ , and  $\zeta_C(E_B)$ . The  $\zeta_V(E_B)$  functional increases in magnitude with decreasing  $E_B$  from the Fermi level to -1.5 eV, indicating that the nonbonding Br 4p states contribute strongly to the SHG response in the VB part. Besides, the drastic change from CBM to 3.6 eV of the  $\zeta_C(E_B)$  functional reveals the essential contribution from the unoccupied Pb-5p states. These results suggest that the SHG responses of these two HOIPs are determined largely by the occupied nonbonding orbitals Br 4p as well as by the unoccupied orbitals Pb 5p from the inorganic layer instead of the organic components.

The quantitative contribution  $A_{\tau}$  (in %) of an individual atom  $\tau$  to the strongest SHG coefficient d<sub>25</sub> for [R-MePEA][C3A]PbBr<sub>4</sub> and [R-MePEA][C4A]PbBr<sub>4</sub> is obtained based on the partial response functional (PRFs). As presented in Table 2, the  $A_{\tau}$  of Pb (~19.9%) in [R-MePEA][C3A]PbBr<sub>4</sub> is nearly 4.6 times that of Br ( $\sim$ 4.3%) and 14.1 times that of N ( $\sim$ 1.4%). Besides, the averaged  $A_{\tau}$  values of C and H are negligibly small, <0.4%. These results reflect that Pb and Br serve as the NLO-active centers at the atomic scale. Considering the number of atoms of each element in the unit cell, the total contributions of Pb, Br, H, C, and N in [R-MePEA][C3A]PbBr<sub>4</sub> are 39.8, 34.5, 11.4, 8.7, and 5.6%. Although the uneven stoichiometry effect is included, the metal atom Pb is still the leading contributor to the SHG response, followed by Br atoms. An identical order of elemental contributions to the total SHG response, Pb > Br > H > C > N, can be seen in [R-MePEA][C4A]PbBr<sub>4</sub>. For both compounds, the contribution of Pb atoms in the valence band can be attributed to the localized Pb 6s and 5d states, while the conduction band contribution mainly originates from the unoccupied Pb 5p states. These findings further quantitatively show that the SHG of [R-MePEA][C3A]PbBr<sub>4</sub> and [R-MePEA][C4A]PbBr<sub>4</sub> mainly originated from the occupied states of Br 4p, Pb 5s, and Pb 5d, and by the unoccupied states of Pb 5p.

Additionally, we note that the  $A_{\tau}$  values of Br atoms vary by their atomic sites. For both compounds (Table 2), the total contributions of SHG for Br1 and Br2 within the ab plane are larger than those of Br3 and Br4 atoms along the c axis. This fact can be interpreted by an analysis of their bonding status, PRF and PDOS, as shown in Figures 2e,f, S2 and S3, respectively. In the top VBs (-1.5 to  $E_F$ ), the nonbonding states from all Br atoms make a strong positive contribution to the SHG response. However, from -2.2 to -1.5 eV in VB

where the Br3(Br4) 4p states make strong bonding interaction with Pb atoms, the PRF  $\zeta_V(E_B)$  decrease sharply with decreasing  $E_B$ . Similarly, a quick drop of the  $\zeta_C(E_B)$ functional can be found from 3.6 to 4.2 eV in CB, where strong Pb-Br3(Br4) antibonding states dominate. Both features show opposite responses in these two energy ranges with respect to the PRF at top VBs or bottom CBs, indicating negative contributions from Br3 and Br4 atoms to the SHG response. Besides, in the bonding region related to Br1 and Br2 atoms, the  $\zeta_V(E_B)$  functional changes little, which implies small contributions from these bonding states. Therefore, the total contribution of SHG for Br3 and Br4 is relatively smaller than that of Br1 and Br2. The reason for such negative contributions is not clear yet, but it may relate to the orbital orientations and the Br...NH noncovalent interactions. Additionally, we found the individual SHG contribution of the Br3 atom is lower than that of Br4 in both compounds. This may be caused by the fact that the covalent bonding strength of Pb-Br3 is stronger than that of Pb-Br4, as the SHG contribution of an individual anion can be weakened when it forms stronger covalent bonds with its surrounding cations.<sup>60</sup>

According to the individual atomic contribution to the SHG response, the contribution of an atomic group can be calculated by summing the contributions of the center atom and those of its ligands. Therefore, the group contribution of PbBr<sub>4</sub> to the SHG response is calculated as follows,

$$\chi_{[PbBr_{6}]}^{(2)} = \chi_{Pb}^{(2)} + 2 \times (\chi_{Br1}^{(2)}/2) + 2 \times (\chi_{Br2}^{(2)}/2) + 1 \times \chi_{Br3}^{(2)} + 1 \times \chi_{Br4}^{(2)}$$
(1)

The total group contributions for the largest second harmonic generation component  $d_{25}$  of [R-MePEA][C3A]-PbBr<sub>4</sub> and [R-MePEA][C4A]PbBr<sub>4</sub> are shown in Figure 3, which shows that the metal-centered groups [PbBr<sub>6</sub>] contribute much more strongly to the SHG response than the organic ligand. That is, the total contribution of the inorganic part for [R-MePEA][C3A]PbBr<sub>4</sub> and [R-MePEA]-[C4A]PbBr<sub>4</sub> is  $\sim$ 72.3 and 83.6%, which far surpasses that of the organic part (i.e., ~25.7, 16.4%), respectively. Our results confirm that the inorganic layer contributes dominantly to the SHG response, while the organic part is important in the stabilization of the crystal structure. Additionally, one can note that the total contribution of the inorganic part in [R-MePEA][C3A]PbBr<sub>4</sub> is relatively smaller than that in [R-MePEA][C4A]PbBr<sub>4</sub>. This indicates that the contribution from the [PbBr<sub>6</sub>] inorganic part to SHG is more significant in the latter compound, which may imply that a longer carbon chain in the organic part results in a reduced contribution to SHG. This could explain why [R-MePEA][C4A]PbBr<sub>4</sub> exhibits a lower SHG response compared to [R-MePEA][C3A]PbBr<sub>4</sub>. Thus, although the mixing of chiral and achiral organic cations contributes to "chiralize" the entire crystal, thus activating the SHG response, further optimization of the NLO properties is

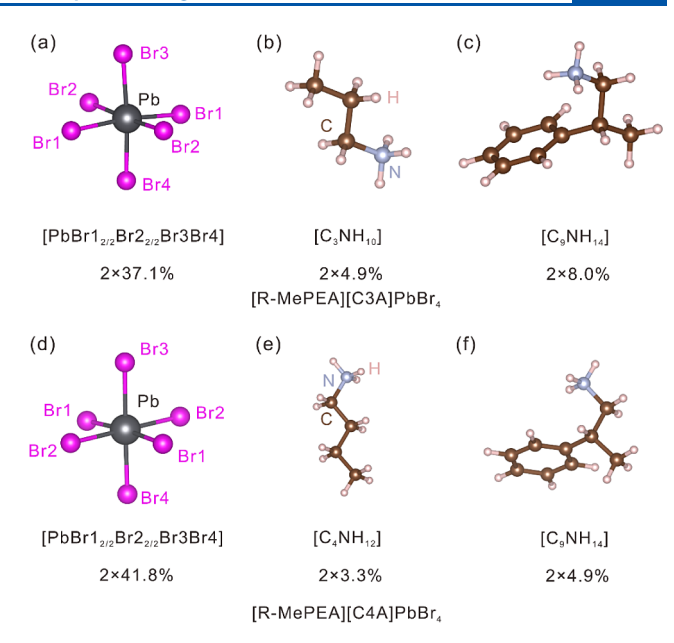


**Figure 3.** Group contributions to the largest second harmonic generation component  $d_{25}$  of [R-MePEA][C3A]PbBr<sub>4</sub> (a-c) and [R-MePEA][C4A]PbBr<sub>4</sub> (d-f).

mainly due to the electronic properties of the framework. At the same time, this suggests that they may additionally be modified by exploiting the tuning of the organic cations, which are affecting the properties of the framework through hydrogen-bonding-induced structural distortions, i.e., chirality transfer.

### 4. CONCLUSION

The structural relaxation, electronic structures, and nonlinear optical properties of alkyl-aryl mixed cation 2D HOIPs, [R-MePEA][C3A]PbBr<sub>4</sub> and [R-MePEA][C4A]PbBr<sub>4</sub>, were studied using first-principles calculations based on DFT. The electronic band gaps were calculated at different approximations, e.g., standard DFT, SOC, and HSE. We find that the presence of Br...NH noncovalent interactions is important in the description of the organic and inorganic hybrid compounds. The calculated DOS, band structures, and COHP show that the top VBs are dominated by nonbonding Br 4p states, while the bottom CBs are made up of unoccupied Pb 6p states and minority C 2p orbitals. The static effective SHG values of [R-MePEA][C3A]PbBr<sub>4</sub> and [R-MePEA]-[C4A]PbBr<sub>4</sub> were calculated as 0.493, and 0.173 pm/V, respectively (i.e.,  $\sim$ 1.49 and 0.53  $\times$   $d_{\rm eff}^{\rm KDP}$ ), which are relatively strong compared with other lead-containing HOIPs. Besides, these two compounds also show a moderate birefringence value  $(\Delta n)$  at 1064 nm. The relatively wide band gaps, SHG responses, and moderate birefringence of the two OIHMHs might suggest that they are suitable for applications in nonlinear optical materials. Furthermore, the total contributions of the inorganic part for [R-MePEA][C3A]PbBr<sub>4</sub> and [R-MePEA][C4A]PbBr<sub>4</sub> are  $\sim$ 72.3 and 83.6%, which far surpasses that of the organic part (i.e.,  $\sim 25.7$ , 16.4%), respectively, reflecting that the inorganic part contributes dominantly to SHG response, while the organic part is important in the stabilization of the crystal structure. Our study suggests that mixed organic chiral 2D HOIPs are potentially good candidates for NLO properties. Further study in this direction

is required from both the experimental and theoretical sides in order to enhance or optimize their NLO responses.

### ASSOCIATED CONTENT

## Supporting Information

The Supporting Information is available free of charge at https://pubs.acs.org/doi/10.1021/acs.jpcc.4c02520.

Details for the PRF method and ART analysis; comparison of the relaxed and experimental structures; electronic structures, COHP analysis, and optical properties for [R-MePEA][C4A]PbBr<sub>4</sub>; calculated ORD and ECD spectra of the neutral and cationic MePEA enantiomers (PDF)

#### AUTHOR INFORMATION

#### **Corresponding Authors**

Shuiquan Deng — State Key Laboratory of Structural Chemistry, Fujian Institute of Research on the Structure of Matter (FJIRSM), Chinese Academy of Sciences (CAS), Fuzhou 350002, P. R. China; orcid.org/0000-0001-5538-6738; Email: sdeng@fjirsm.ac.cn

Alessandro Stroppa — CNR-SPIN, Coppito (AQ) 67100, Italy; orcid.org/0000-0001-6067-0434; Email: alessandro.stroppa@spin.cnr.it

#### **Authors**

- Xiyue Cheng State Key Laboratory of Structural Chemistry, Fujian Institute of Research on the Structure of Matter (FJIRSM), Chinese Academy of Sciences (CAS), Fuzhou 350002, P. R. China; orcid.org/0000-0003-2440-394X
- S. Muthukrishnan Computational Laboratory for Multifunctional Materials (CoLaMM), Department of Physics and Centre for Materials Informatics (C-MaIn), Sir C V Raman Science Block, Anna University, Chennai 600025, India
- Hanxiang Mi State Key Laboratory of Structural Chemistry, Fujian Institute of Research on the Structure of Matter (FJIRSM), Chinese Academy of Sciences (CAS), Fuzhou 350002, P. R. China
- Goncagül Serdaroğlu Faculty of Education, Sivas Cumhuriyet University, Sivas 58140, Turkey
- R. Vidya Computational Laboratory for Multifunctional Materials (CoLaMM), Department of Physics and Centre for Materials Informatics (C-MaIn), Sir C V Raman Science Block, Anna University, Chennai 600025, India

Complete contact information is available at: https://pubs.acs.org/10.1021/acs.jpcc.4c02520

#### **Author Contributions**

\*X.C. and S.M. contributed equally to this work. A.S. and S.D. proposed the project. X.C., S.M., and H.M. performed the calculations. The manuscript was written through the contributions of all authors.

#### Notes

The authors declare no competing financial interest.

## ACKNOWLEDGMENTS

The work at FJIRSM was financially supported by the National Natural Science Foundation (NSF) of China (22031009, 21921001, 22075282); the National Key R&D Program of China (2021YFB3601501); the NSF of Fujian Province (2023J01212). The work has been performed under Project

HPC-EUROPA3 (HPC17Y3BP5 and HPC17P14RF), with the support of the EC Research Innovation Action under the H2020 Programme; CNR-SPIN, the Italian National Research Council Institute for Superconductors, with HPC resources and support provided by Cineca. We acknowledge support from the Italian Ministry of Research under the PRIN 2022 Grant No. 2022F2K7J5 with title Two dimensional chiral hybrid organic—inorganic perovskites for chiroptoelectronics PE 3 funded by PNRR Mission 4 Istruzione e Ricerca-Component C2- Investimento 1.1, Fondo per il Programma Nazionale di Ricerca e Progetti di Rilevante Interesse Nazionale PRIN 2022 -CUP B53D23004130006. A.S. thanks the support from bilateral project CNR e NSFC (Cina), "Ferroelectric and chiral hybrid organic-inorganic perovskites", biennio 2024-2025").

#### REFERENCES

- (1) Ehrlich, P.; Einhorn, A. Ueber die physiologische Wirkung der Verbindungen der Cocainreihe. *Berichte* **1894**, *27*, 1870–1873.
- (2) Pictet, A.; Rotschy, A. Synthese des Nicotins. Berichte 1904, 37, 1225-1235
- (3) Guijarro, A.; Yus, M. The Origin of Chirality in the Molecules of Life: From Awareness to the Current Theories and Perspectives of this Unsolved Problem; Royal society of Chemistry, 2009.
- (4) Pietropaolo, A.; Nakano, T. Molecular mechanism of polyacrylate helix sense switching across its free energy landscape. *J. Am. Chem. Soc.* **2013**, *135* (15), 5509–5512.
- (5) Aucar, J. J.; Stroppa, A.; Aucar, G. A. A relationship between the molecular parity-violation energy and the electronic chirality measure. *J. Phys. Chem. Lett.* **2024**, *15* (1), 234–240.
- (6) Mao, L.; Stoumpos, C. C.; Kanatzidis, M. G. Two-Dimensional Hybrid Halide Perovskites: Principles and Promises. *J. Am. Chem. Soc.* **2019**, *141* (3), 1171–1190.
- (7) Brenner, T. M.; Egger, D. A.; Kronik, L.; Hodes, G.; Cahen, D. Hybrid organic—inorganic perovskites: Low-cost semiconductors with intriguing charge-transport properties. *Nat. Rev. Mater.* **2016**, *1* (1), 15007.
- (8) Saparov, B.; Mitzi, D. B. Organic-Inorganic Perovskites: Structural Versatility for Functional Materials Design. *Chem. Rev.* **2016**, *116* (7), 4558–4596.
- (9) Hu, J.; Oswald, I. W. H.; Hu, H.; Stuard, S. J.; Nahid, M. M.; Yan, L.; Chen, Z.; Ade, H.; Neilson, J. R.; You, W. Aryl-Perfluoroaryl Interaction in Two-Dimensional Organic-Inorganic Hybrid Perovskites Boosts Stability and Photovoltaic Efficiency. *ACS Mater. Lett.* **2019**, *1* (1), 171–176.
- (10) Mitzi, D. B.; Medeiros, D. R.; Malenfant, P. R. L. Intercalated Organic-Inorganic Perovskites Stabilized by Fluoroaryl-Aryl Interactions. *Inorg. Chem.* **2002**, *41* (8), 2134–2145.
- (11) Yan, L.; Hu, J.; Zhou, N.; Moran, A. M.; You, W. Enhancing Photovoltaic Performance of Aromatic Ammonium-based Two-Dimensional Organic-Inorganic Hybrid Perovskites via Tuning  $CH\cdots\pi$  Interaction. Sol. RRL 2020, 4 (1), 1900374.
- (12) Qiu, J.; Xia, Y.; Zheng, Y.; Hui, W.; Gu, H.; Yuan, W.; Yu, H.; Chao, L.; Niu, T.; Yang, Y.; Gao, X.; Chen, Y.; Huang, W. 2D Intermediate Suppression for Efficient Ruddlesden-Popper (RP) Phase Lead-Free Perovskite Solar Cells. ACS Energy Lett. 2019, 4 (7), 1513–1520.
- (13) Lian, X.; Chen, J.; Qin, M.; Zhang, Y.; Tian, S.; Lu, X.; Wu, G.; Chen, H. The Second Spacer Cation Assisted Growth of a 2D Perovskite Film with Oriented Large Grain for Highly Efficient and Stable Solar Cells. *Angew. Chem., Int. Ed.* **2019**, 58 (28), 9409–9413. (14) Zhou, N.; Huang, B.; Sun, M.; Zhang, Y.; Li, L.; Lun, Y.; Wang, X.; Hong, J.; Chen, Q.; Zhou, H. The Spacer Cations Interplay for Efficient and Stable Layered 2D Perovskite Solar Cells. *Adv. Energy Mater.* **2020**, 10 (1), 1901566.

- (15) Long, G.; Sabatini, R.; Saidaminov, M. I.; Lakhwani, G.; Rasmita, A.; Liu, X.; Sargent, E. H.; Gao, W. Chiral-perovskite optoelectronics. *Nat. Rev. Mater.* **2020**, 5 (6), 423–439.
- (16) Dang, Y.; Liu, X.; Cao, B.; Tao, X. Chiral halide perovskite crystals for optoelectronic applications. *Matter* **2021**, *4* (3), 794–820.
- (17) Kim, Y.-H.; Zhai, Y.; Lu, H.; Pan, X.; Xiao, C.; Gaulding, E. A.; Harvey, S. P.; Berry, J. J.; Vardeny, Z. V.; Luther, J. M.; et al. Chiral-induced spin selectivity enables a room-temperature spin light-emitting diode. *Science* **2021**, *371* (6534), 1129–1133.
- (18) Ma, J.; Fang, C.; Chen, C.; Jin, L.; Wang, J.; Wang, S.; Tang, J.; Li, D. Chiral 2D Perovskites with a High Degree of Circularly Polarized Photoluminescence. ACS Nano 2019, 13 (3), 3659–3665.
- (19) Ishii, A.; Miyasaka, T. Direct detection of circular polarized light in helical 1D perovskite-based photodiode. *Sci. Adv.* **2020**, *6* (46), No. eabd3274.
- (20) Yang, C.-K.; Chen, W.-N.; Ding, Y.-T.; Wang, J.; Rao, Y.; Liao, W.-Q.; Tang, Y.-Y.; Li, P.-F.; Wang, Z.-X.; Xiong, R.-G. The First 2D Homochiral Lead Iodide Perovskite Ferroelectrics: [R- and S-1-(4-Chlorophenyl) ethylammonium]2PbI4. *Adv. Mater.* **2019**, *31* (16), 1808088.
- (21) Xu, J.; Li, X.; Xiong, J.; Yuan, C.; Semin, S.; Rasing, T.; Bu, X.-H. Halide Perovskites for Nonlinear Optics. *Adv. Mater.* **2020**, *32*, 1806736
- (22) Han, X.; Zheng, Y.; Chai, S.; Chen, S.; Xu, J. 2D organic-inorganic hybrid perovskite materials for nonlinear optics. *Nano-photonics* **2020**, *9*, 1787–1810.
- (23) Reshak, A. H.; Auluck, S. Two Haloid Borate Crystals with Large Nonlinear Optical Response. *Phys. Chem. Chem. Phys.* **2017**, *19*, 18416–18425.
- (24) Reshak, A. H.; Auluck, S. The Influence of Oxygen Vacancies on the Linear and Nonlinear Optical Properties of Pb<sub>7</sub>O-(OH)<sub>3</sub>(CO<sub>3</sub>)<sub>3</sub>(BO<sub>3</sub>). RSC Adv. **2017**, 7, 14752–14760.
- (25) Reshak, A. H.; Abbass, N. M.; Bila, J.; Johan, M. R.; Kityk, I. Noncentrosymmetric Sulfide Oxide Mznso (M = Ca or Sr) with Strongly Polar Structure as Novel Nonlinear Crystals. *J. Phys. Chem. C* **2019**, *123*, 27172–27180.
- (26) Yan, L.; Jana, M. K.; Sercel, P. C.; Mitzi, D. B.; You, W. Alkyl-Aryl Cation Mixing in Chiral 2D Perovskites. *J. Am. Chem. Soc.* **2021**, 143 (43), 18114–18120.
- (27) Kresse, G.; Hafner, J. Ab-initio molecular dynamics for liquid metals. *Phys. Rev. B* **1993**, *47*, 558.
- (28) Kresse, G.; Furthmuller, J. Efficient iterative schemes for ab initio total-energy calculations using a plane-wave basis set. *J. Phys. Chem. B* **1996**, *54*, 11169–11186.
- (29) Kresse, G.; Furthmuller, J. Efficiency of ab-initio total energy calculations for metals and semiconductors using a plane-wave basis set. *Comput. Mater. Sci.* **1996**, *6*, 15–50.
- (30) Perdew, J. P.; Burke, K.; Ernzerhof, M. Generalized gradient approximation made simple. *Phys. Rev. Lett.* **1996**, 77 (18), 3865–3868.
- (31) Perdew, J. P.; Wang, Y. Accurate and simple analytic representation of the electron-gas correlation-energy. *Phys. Rev. B* **1992**, 45, 13244–13249.
- (32) Cheng, X. Y.; Whangbo, M.-H.; Guo, G.-C.; Hong, M. C.; Deng, S. Q. The Large Second-Harmonic Generation of LiCs<sub>2</sub>PO<sub>4</sub> is caused by the Metal-Cation-Centered Groups. *Angew. Chem., Int. Ed.* **2018**, *57*, 3933–3937.
- (33) Aversa, C.; Sipe, J. E. Nonlinear-Optical Susceptibilities of Semiconductors Results with a Length-Gauge Analysis. *Phys. Rev. B* **1995**, *52*, 14636–14645.
- (34) Rashkeev, S. N.; Lambrecht, W. R. L.; Segall, B. Efficient ab initio method for the calculation of frequency-dependent second-order optical response in semiconductors. *Phys. Rev. B* **1998**, *57*, 3905–3919.
- (35) Rashkeev, S. N.; Lambrecht, W. R. L. Second-harmonic generation of I-III-VI2 chalcopyrite semiconductors: Effects of chemical substitutions. *Phys. Rev. B* **2001**, *63*, 165212–165223.

- (36) Sharma, S.; Dewhurst, J. K.; Ambrosch-Draxl, C. Linear and second-order optical response of III-V monolayer superlattices. *Phys. Rev. B* **2003**, *67*, 165332–165340.
- (37) Sharma, S.; Ambrosch-Draxl, C. Second-harmonic optical response from first principles. *Phys. Scr.* **2004**, *T109*, 128–134.
- (38) Gonze, X.; Lee, C. Dynamical matrices, Born effective charges, dielectric permittivity tensors, and interatomic force constants from density-functional perturbation theory. *Phys. Rev. B* **1997**, *55*, 10355–10368.
- (39) Heyd, J.; Peralta, J. E.; Scuseria, G. E.; Martin, R. L. Energy band gaps and lattice parameters evaluated with the Heyd-Scuseria-Ernzerhof screened hybrid functional. *J. Chem. Phys.* **2005**, *123*, 174101.
- (40) Paier, J.; Marsman, M.; Hummer, K.; Kresse, G.; Gerber, I. C.; Angyan, J. G. Screened hybrid density functionals applied to solids. *J. Chem. Phys.* **2006**, *124*, 154709.
- (41) Krukau, A. V.; Vydrov, O. A.; Izmaylov, A. F.; Scuseria, G. E. Influence of the exchange screening parameter on the performance of screened hybrid functionals. *J. Chem. Phys.* **2006**, *125*, 224106.
- (42) Kurtz, S. K.; Perry, T. T. A Powder Technique for the Evaluation of Nonlinear Optical Materials. *J. Appl. Phys.* **1998**, 39, 3798–3813.
- (43) Cyvin, S. J.; Rauch, J. E.; Decius, J. C. Theory of Hyper-Raman Effects (Nonlinear Inelastic Light Scattering)- Selection Rules and Depolarization Ratios for Second-Order Polarizability. *J. Chem. Phys.* **1965**, *43*, 4083–4095.
- (44) Frisch, M. J.; Trucks, G. W.; Schlegel, H. B.; Scuseria, M. A.; Robb, M. A.; Cheeseman, J. R.; Scalmani, G.; Barone, V.; Mennucci, B.; Petersson, G. A., et al. Gaussian 09W. *Revision D.01*; Gaussian, Inc: Wallingford CT, 2013.
- (45) Becke, A. D. A new mixing of Hartree–Fock and local density-functional theories. *J. Chem. Phys.* **1993**, 98, 1372–1377.
- (46) Lee, C.; Yang, W.; Parr, R. G. Development of the Colle-Salvetti correlation-energy formula into a functional of the electron density. *Phys. Rev.* **1988**, *B37*, 785–789.
- (47) Hinchliffe, A. CS Chem3D Pro 3.5 and CS MPAC Pro (MAC and windows) UK. Electron. J. Theor. Chem. 1997, 2, 215–217.
- (48) de la Flor, G.; Orobengoa, D.; Tasci, E.; Perez-Mato, J. M.; Aroyo, M. I. Comparison of structures applying the tools available at the Bilbao Crystallographic Server. *J. Appl. Crystallogr.* **2016**, 49, 653–664
- (49) Maintz, S.; Deringer, V. L.; Tchougreeff, A. L.; Dronskowski, R. LOBSTER: A tool to extract chemical bonding from plane-wave based DFT. *J. Comput. Chem.* **2016**, *37*, 1030–1035.
- (50) Dronskowski, R.; Bloechl, P. E. Crystal orbital Hamilton populations (COHP): energy-resolved visualization of chemical bonding in solids based on density-functional calculations. *J. Phys. Chem.* **1993**, 97, 8617–8624.
- (51) Jia, M.; Cheng, X.; Whangbo, M.-H.; Hong, M.; Deng, S. Second harmonic generation responses of KH2PO4: Importance of K and breaking down of Kleinman symmetry. *RSC Adv.* **2020**, *10*, 26479–26485.
- (52) Yang, M.; Cheng, H.; Xu, Y.; Li, M.; Ai, Y. A hybrid organic-inorganic perovskite with robust SHG switching. *Chin. Chem. Lett.* **2022**, 33, 2143–2146.
- (53) Mączka, M.; Zaręba, J. K.; Gągor, A.; Stefańska, D.; Ptak, M.; Roleder, K.; Kajewski, D.; Soszyński, A.; Fedoruk, K.; Sieradzki, A. [Methylhydrazinium]2PbBr4, a Ferroelectric Hybrid Organic–Inorganic Perovskite with Multiple Nonlinear Optical Outputs. *Chem. Mater.* **2021**, 33, 2331–2342.
- (54) Mączka, M.; Ptak, M.; Gągor, A.; Stefańska, D.; Zaręba, J. K.; Sieradzki, A. Methylhydrazinium Lead Bromide: Noncentrosymmetric Three-Dimensional Perovskite with Exceptionally Large Framework Distortion and Green Photoluminescence. *Chem. Mater.* **2020**, 32, 1667–1673.
- (55) Li, L.; Liu, X.; Li, Y.; Xu, Z.; Wu, Z.; Han, S.; Tao, K.; Hong, M.; Luo, J.; Sun, Z. Two-Dimensional Hybrid Perovskite-Type Ferroelectric for Highly Polarization-Sensitive Shortwave Photodetection. J. Am. Chem. Soc. 2019, 141, 2623–2629.

- (56) Yuan, C.; Li, X.; Semin, S.; Feng, Y.; Rasing, T.; Xu, J. Chiral Lead Halide Perovskite Nanowires for Second-Order Nonlinear Optics. *Nano Lett.* **2018**, *18*, 5411–5417.
- (57) Huang, Z.; Bloom, B. P.; Ni, X.; Georgieva, Z. N.; Marciesky, M.; Vetter, E.; Liu, F.; Waldeck, D. H.; Sun, D. Magneto-Optical Detection of Photoinduced Magnetism via Chirality-Induced Spin Selectivity in 2D Chiral Hybrid Organic—Inorganic Perovskites. *ACS Nano* 2020, *14*, 10370–10375.
- (58) Sun, B.; Liu, X.-F.; Li, X.-Y.; Zhang, Y.; Shao, X.; Yang, D.; Zhang, H.-L. Two-Dimensional Perovskite Chiral Ferromagnets. *Chem. Mater.* **2020**, 32, 8914–8920.
- (59) Georgieva, Z. N.; Bloom, B. P.; Ghosh, S.; Waldeck, D. H. Imprinting Chirality onto the Electronic States of Colloidal Perovskite Nanoplatelets. *Adv. Mater.* **2018**, *30*, 1800097.
- (60) Cheng, X.; Li, Z. H.; Wu, X.-T.; Hong, M.; Whangbo, M.-H.; Deng, S. Key factors controlling the large second harmonic generation in nonlinear optical materials. *ACS Appl. Mater. Interfaces* **2020**, *12*, 9434–9439.



CAS BIOFINDER DISCOVERY PLATFORM™

## BRIDGE BIOLOGY AND CHEMISTRY FOR FASTER ANSWERS

Analyze target relationships, compound effects, and disease pathways

**Explore the platform** 

